LS-DYNA® Implemented Multi-Layer Fabric Material Model Development for Engine Fragment Mitigation

S. D. Rajan, B. Mobasher and A. Vaidya

Civil, Environmental & Sustainable Engineering Program

Arizona State University

Tempe, AZ 85287

Abstract

The development of a robust and reliable material model for dry fabrics is the main subject of this paper. Dry fabrics are used in a number of applications such as propulsion engines fan-containment systems, and soft body armor. A mechanistic-based material behavior model capturing the behavior of fabrics when subjected to impacts from high-velocity projectiles would make a powerful predictive tool. In this paper, the constitutive model for Kevlar® 49 is developed. Experimental static and high strain rate tensile tests have been conducted at Arizona State University (ASU) to obtain the material properties of Kevlar fabric. Results from laboratory tests such as Tension Tests including high-strain rate tests, Picture Frame Shear Tests, and Friction Tests yield most of the material properties needed to define a constitutive model. The material model is incorporated in the LS-DYNA commercial program as a user-defined subroutine. The validation of the model is carried out by numerically simulating actual ballistic tests conducted at NASA-GRC.

1.0 Introduction

High strength woven fabrics are ideal candidate materials for use in structural systems where high energy absorption is required. Their high strength to weight ratio and the ability to resist high speed fragment impacts enable them to be very efficient compared to metals. One of the more widely used applications for woven fabrics is in propulsion engine containment systems. The engine containment system is typically constructed by wrapping multiple layers of Kevlar®49 around a thin aluminum encasement (Fig. 1). The fabric is then covered with a protective layer.

Figure 1. Honeywell engine

Designing the containment system consists of determining the type of fabric, the number of fabric layers and fabric width required. Currently the FAA's certification standards require that a full-scale test be completed to qualify an engine. Because of the extensive pre and post-test analysis, and the fact that equipment is unusable after testing, a typical fan blade out (FBO) test can cost several million dollars. With today's advanced numerical techniques, modeling a propulsion engine and simulating a FBO event can be accomplished using an appropriate hydrocode. While there are proven constitutive models that can simulate the behavior of most of the materials [Ishikawa and Chou, 1982; Scida et al., 1999; Jiang et. al., 2000], the difficulty lies

in the fact that there is no mechanistic based constitutive model for woven Kevlar®49 (or any other) fabric, especially one that can be used to predict the fabric's behavior when subjected to high-speed impact loads. The challenge is to represent the actual fabric as an equivalent continuum element as shown in Fig. 2.
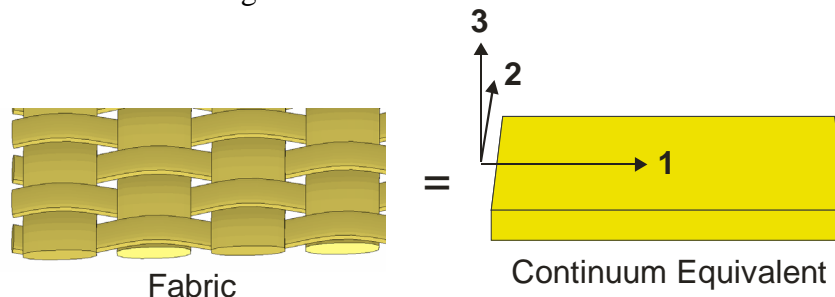

Figure 2. Modeling the dry fabric as a continuum

2.0 Experimental Program for Constitutive Model

Our constitutive model is developed using a combination of experimental test data and virtual testing [Naik et. al., 2009; Stahlecker et. al., 2009]. We take material direction 11 as the main longitudinal direction of the fabric (warp direction), direction 22 as the direction along the width of the fabric (fill direction), and direction 33 refers to the direction perpendicular to both warp and fill directions. The fabric has negligible stiffness perpendicular to both fabric material directions and hence those properties were assumed to be zero. The constitutive behavior suitable for use in an explicit finite element analysis in stiffness incremental form is shown below.

$$
\begin{bmatrix} \Delta\sigma_{11} \\ \Delta\sigma_{22} \\ \Delta\sigma_{33} \\ \Delta\sigma_{12} \\ \Delta\sigma_{31} \\ \Delta\sigma_{23} \end{bmatrix} = \begin{bmatrix} E_{11} & 0 & 0 & 0 & 0 & 0 \\ 0 & E_{22} & 0 & 0 & 0 & 0 \\ 0 & 0 & 0 & 0 & 0 & 0 \\ 0 & 0 & 0 & 2G_{12} & 0 & 0 \\ 0 & 0 & 0 & 0 & 2G_{31} & 0 \\ 0 & 0 & 0 & 0 & 0 & 2G_{23} \end{bmatrix} \begin{bmatrix} \Delta\varepsilon_{11} \\ \Delta\varepsilon_{22} \\ \Delta\varepsilon_{33} \\ \Delta\varepsilon_{12} \\ \Delta\varepsilon_{31} \\ \Delta\varepsilon_{23} \end{bmatrix}
\tag{1}
$$

No coupling effect between the material directions was assumed – the Poisson's ratios were assumed to be zero. Gasser and co-workers [Gasser et. al, 2000] using biaxial tests and three-dimensional finite element simulations show that v_{12}, v_{13} and v_{23} are negligibly small. The decoupled stress-strain relationship has been successfully used to model dry fabric structural systems [Duana et.al., 2005; Raftenberg, 2004]. E_{33} is taken as zero simply because the shell element formulation (shell elements are used to model the fabric). The values for E_{11}, E_{22}, G_{12}, G_{31}, and G_{23} are a function of several factors including the current stress and strain, the stress and strain history, and the strain rate.

Tensile Behavior
Uniaxial tension tests were conducted in both the warp and fill directions. The results for the warp direction are shown in Fig. 3. The primary mode of failure of Kevlar 49 is the breakage of the warp or fill direction yarns. Hence, once the element representing the fabric experienced a critical level of strain in either the warp or fill directions, the element is considered to have failed

in that direction. To simplify and simulate this in the material model, the post-peak region is approximated with a linear region followed by a non-linear region up until fabric failure (Fig. 3).
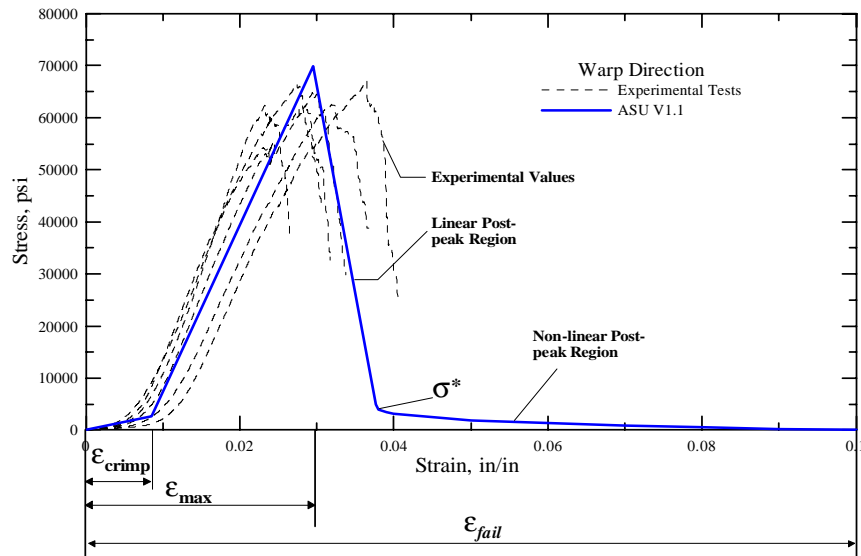
Figure 3. Kevlar® 49 warp (11) direction uniaxial stress-strain results

Unloading/Reloading and Compressive Behavior
When the fabric is subjected to impact loads, it can load and unload many times throughout the event. It is important to determine its cyclic behavior and model it correctly. Cyclic tests in the warp direction for three Kevlar®49 samples were conducted to determine the fabric's unloading and reloading behavior. The test results show that in the elastic region, the fabric unloads and reloads approximately along the same path but at a slope that is about one and a half times the elastic stiffness. In the post-peak region, the unloading and reloading stiffness decreases as the strain increases likely resulting from an increase in the breakage of fibers. The cyclic test fabric samples showed that the warp direction had an average strain at peak stress of approximately 0.0240 whereas the uniaxial test samples showed an average of approximately 0.0295. This could be due to the variability in the stress-strain response of the fabric. Since cyclic testing of the fill direction was not conducted, it was assumed that the unloading and reloading stiffness of the fill direction was similar to the warp direction. For simplicity and due to the lack of experimental data, the unloading and reloading stiffness were assumed to be independent of strain rate.
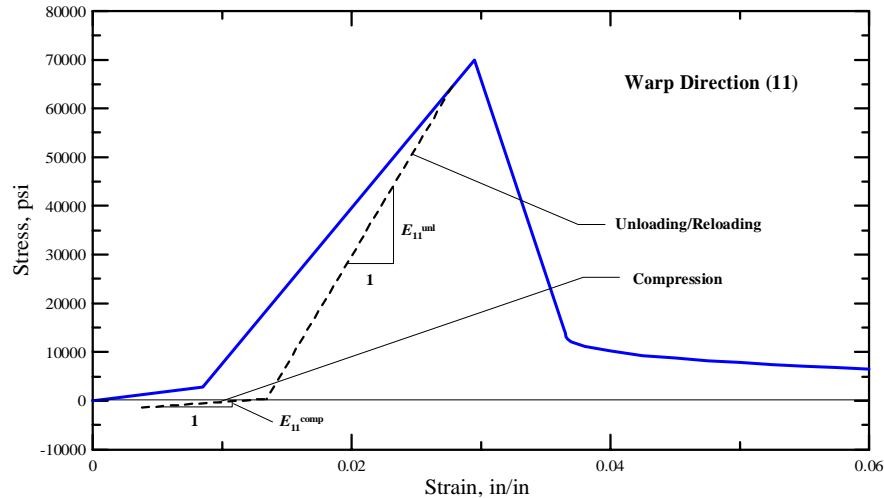
Figure 4. Unloading/Reloading and compression behavior assumed in material model for warp direction

Kevlar®49 fabric has negligible compressive stiffness. If a zero (or numerically tiny) compressive stiffness is used, the model behavior in an explicit finite element analysis is unrealistic – the projectile simply cuts through the fabric. To avoid this problem, a very small stiffness was assumed. The compressive stiffness was taken as 0.5% of the elastic stiffness. Fig. 4 shows the general unloading, reloading, and compressive behavior of the fabric's warp direction as assumed for the constitutive model. A similar behavior is used for the fill direction.

Shear Behavior
The experimental setup is shown in Fig. 5. Typical results are shown in Fig. 6. The shear resistance increases with an increase in shear strain. At low shear strains the fabric has little resistance to shear deformation. The yarns rotate and the warp and fill directions are no longer orthogonal. At some point there is a very rapid increase in the shear stress value. This is caused by the re-orientation and packing of the fabric yarns as the shear strain increases. Initial finite element simulations discussed in the following section were run using shear modulus values based on these results. The simulations were highly inaccurate as the fabric experienced large local deformations around the contact area that were not seen in the experimental tests. A further examination of the fabric's deformation during the tests revealed that the fabric was wrinkling at the edges during the initial stages of loading and experienced buckling during the final stages of loading. Based on these observations, we corrected the shear-stress strain curve to include only the behavior captured by yarn reorientation. In the material model, a piecewise linear approximation of the corrected results is used and is shown in Fig. 6. The fabric is assumed to unload and reload along the same path. The in-plane shear stress increment is computed as follows.

$$\Delta\sigma_{12} = 2\Delta\varepsilon_{12}G_{12} \tag{2}$$

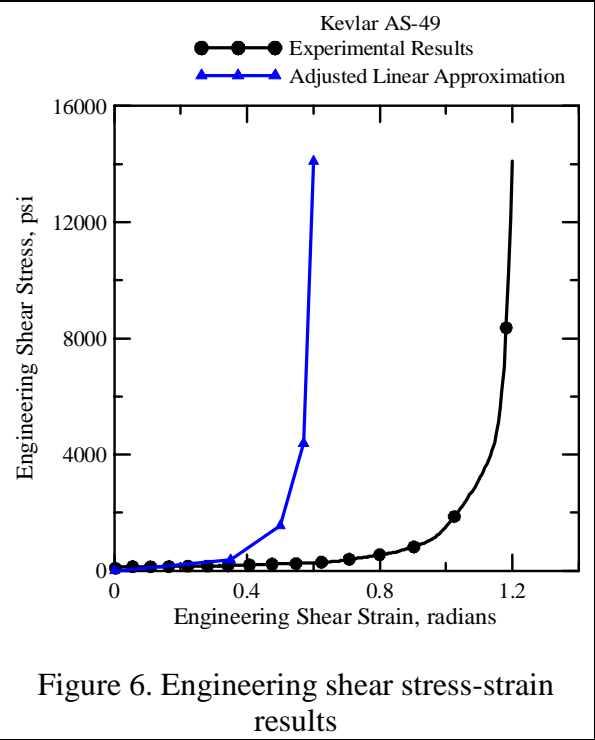Figure 5. Picture frame shear test setup

Figure 6. Engineering shear stress-strain results

Strain Rate Effects

The high strain rate testing system, shown as Fig. 7, includes MTS 5 kip servo-hydraulic tensile testing machine, MTS Flex SE control panels, laser extensometer, and data acquisition system. A typical 2" test specimen is shown in Fig. 8. The high strain rate tests were conducted to about 200/s, the capacity of the machine. Using other publicly available data [Xia and Wang, 1999], the Cowper-Symonds type of strain rate dependent model is constructed as shown in Fig. 9.
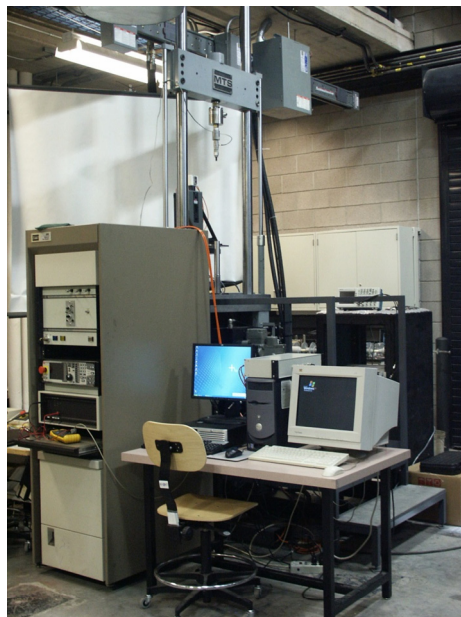

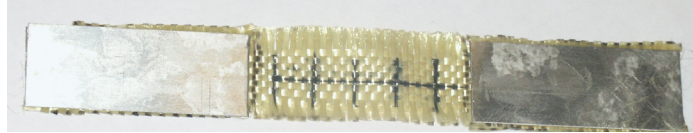Figure 7. High strain-rate test setup
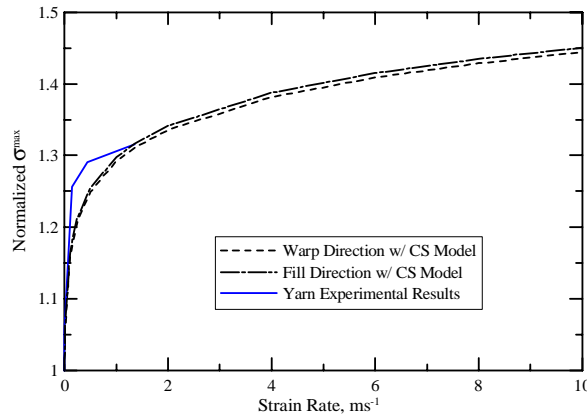
Figure 8. Test specimen

Figure 9. Normalized peak stress as a function of strain rate

Fabric-on-fabric Friction Tests

The test setup is shown in Fig. 10. For the experiment, a layer of fabric was pulled using a 55 kip horizontal actuator. This fabric layer was sandwiched between another layer of the same fabric. Normal loads were applied on the fabrics such that the maximum normal load was 800 pounds for a contact area of 13.75 square inches (60 psi). These normal loads were applied through another actuator mounted vertically on an I beam resting on to channel sections connected to the four columns as shown in figure 10. The second layer of fabric was allowed to move using zinc ball joint rod ends that were fixed to an I-beam. Fig. 11 shows the coefficient of the friction for samples tested with a loading rate of 2.0 inches per minute.

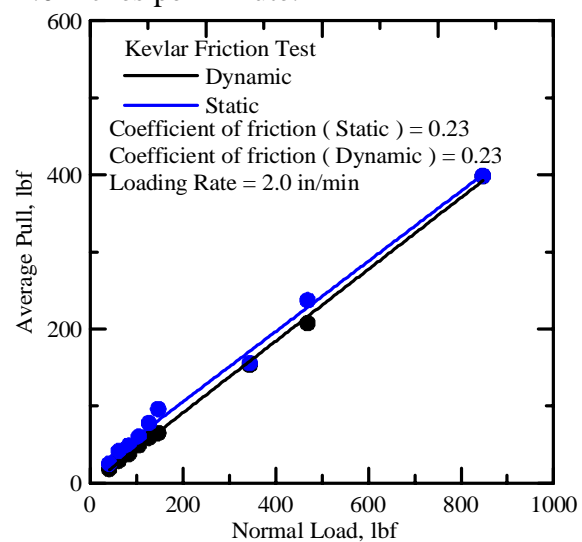Figure 10. Friction Test setup

Figure 11. Coefficient of friction for loading rate of 2.0 in/min

3.0 Ballistic Tests

To validate the developed constitutive model that is implemented in LS-DYNA as a user-supplied material model, ballistic tests were carried out at NASA-GRC using a gas gun and aiming a steel projectile at a ring wrapped with Kevlar fabric (see Fig. 12). The event was monitored closely including taking pictures using a high-speed camera. A total of 20 tests were carried out where the number of fabric layers, the projectile velocity and orientations were varied.
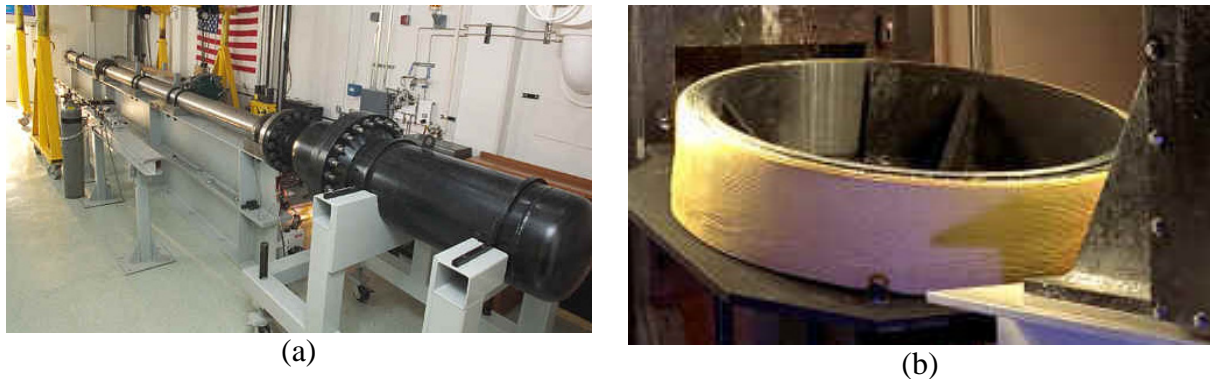

(a) (b)

Fig. 12. Ballistic Test Setup (a) Gas gun (b) Steel ring wrapped with several layers of Kevlar

The stainless steel projectiles used in the tests are shown in Fig. 13 and henceforth referred to as old (O) and new (N).
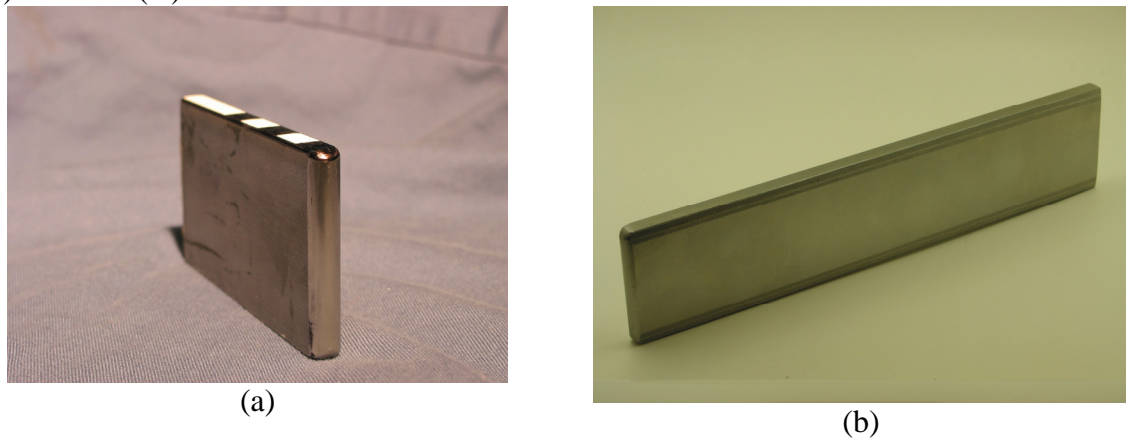

(a) (b)

Figure 13. Stainless steel projectile (a) Old (b) New

The old projectile is a rectangular shaped, 304L stainless steel article, 10.2 cm (4 in) long, 5.1 cm (2 in) high and 0.8 cm (5/16 in) thick, with a nominal mass of 320 gm. The front edge and the corners of the projectile are machined with a full radius. The new projectile is also 304L stainless steel, but had a length of 17.8 cm (7 in), a height of 3.8 cm (1.5 in), a thickness of 0.54 cm (.2135 in) and the same nominal mass as the old projectile. The front edge and corners also were machined with a full radius. The gas gun used to accelerate the projectile consisted of a pressure vessel with a volume of 0.35 m3 (12.5 ft3), a gun barrel with a length of 12.2 m (40 ft) and an inner diameter of 20.32 cm (8 in). A photograph of the gun is shown in Fig. 12(a). The pressure vessel and the gun barrel were mated by a flange on each side with a number of layers of Mylar® sheet sandwiched between the flanges to seal the pressure vessel and act as a burst valve. Helium gas was used as the propellant. The pressurized helium was released into the gun barrel by applying a voltage across a Nichrome wire embedded in the Mylar sheets, causing the Mylar sheets to rupture. The projectile was supported inside an aluminum can-shaped

cylindrical sabot that was machined to fit snugly inside the gun barrel. The orientation of the projectile was controlled by supporting the projectile either with rigid foam or with an aluminum wedge welded to the bottom of the sabot. The sabot was stopped at the end of the gun barrel by a thick steel plate with a rectangular slot large enough to allow the projectile to pass through. The gun barrel was evacuated to reduce blast loading on the specimen and to reduce the amount of pressure required to achieve the desired impact velocity.

4.0 Numerical Results

The FE model of each ballistic test was created using shell finite elements for the fabric and solid finite elements for the steel ring and the projectile. Two models were built – the single FE layer (SL model) refers to the model where a single FE shell element is used to model all the Kevlar fabric layers, the multiple FE layer (ML model) refers to the model where a single FE shell element is used to model 4 Kevlar fabric layers.

The SL model is computationally efficient. On an average, it takes between 25-50% of the wall clock time required for the corresponding ML model. The ML model provides a more detailed picture of the fabric wrap as a containment system and is designed to predict the extent of the fabric wrap damage. For one of the models (LG612), the comparison between the experiment and the FE simulation is shown in Fig. 14. Table 1 shows the summary of the 18 ballistic tests. The absorbed energy is given as

$$E_a = \frac{1}{2}m\left(v_i^2 - v_f^2\right) \tag{3}$$

where m is the mass of the projectile, v_i and v_f are the initial and final velocities respectively. The percent absorbed energy is given as

$$E_a^\% = \frac{\left(v_i^2 - v_f^2\right)}{v_i^2} \times 100 \tag{4}$$

Table 2 shows the comparison between the experimental results and the FE model predictions. The % difference between the experimental and the FE model prediction are computed as

$$D = \left(E_a^\%\right)_{\exp} - \left(E_a^\%\right)_{FE} \tag{5}$$

where *exp* refers to the experimental value and *FE* refers to the FE model value. Hence a positive D corresponds to the FE simulation under predicting the absorbed energy and a negative D corresponds to the FE simulation over predicting the absorbed energy. The results show that the SL model on an average under predicts the absorbed energy. Generally, the predictions are better for smaller number of layers. As the number of layers increases, the predictions get progressively worse with the worst overprediction with LG618 (8 layer model) and the underprediction with LG656 (32 layers). The performance of the ML model is comparatively worse. The two models that define the extreme error values as LG618 where the energy absorbed is overpredicted and LG656 where the energy absorbed is underpredicted.
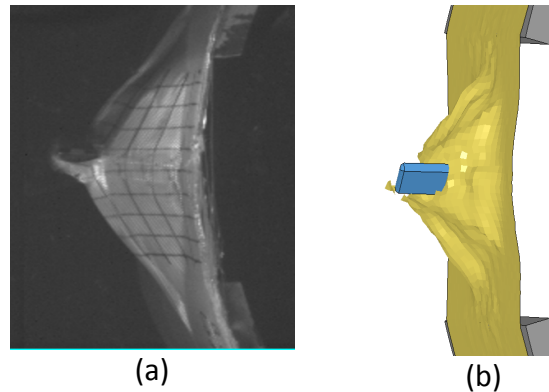
(a)   (b)

Fig. 14. (a) Experimental result (b) FE Simulation for LG612

Finally, the developed model is used as a tool in predicting the ballistic limit. Table 3 shows the results for 4, 12, 16, 24 and 32 layers for a direct hit (zero roll, pitch and yaw values).

The orientation of the projectile was measured from the location of three points on the projectile that defined a local moving coordinate system and three points at a fixed location in the background that defined a laboratory coordinate system. The laboratory coordinate system consisted of the X axis in the direction of the gun axis, a Z axis in the vertical upward direction and Y axis defined by the vector product of Z and X. The orientation of the projectile was defined by a set of three Euler angles defined by a rotation θ (roll), about the laboratory X axis, followed by a rotation ψ (pitch) about the rotated y-axis, followed by a rotation φ (yaw) about the (twice) rotated z-axis. The roll, pitch and yaw angles are defined as the rotation about the e_1 axis, e_2 axis, and the e_3 axis, respectively, as shown in Fig. 15 where the local coordinate system is shown at the center of the projectile. A right hand rule is used to define positive and negative rotations.

Table 1. Ballistic Test Data

Model	Fabric Layers	Projectile Mass (g) & Type (O/N)	Roll, Pitch and Yaw (degrees)	Initial Velocity (ft/s)	Final Velocity (ft/s)	Absorbed Energy (%)
LG404	8	317.8 (O)	0,0,0	895.7	820.2	16.1
LG409	8	316 (O)	0,0,0	889.1	807.1	17.6
LG411	24	314.8 (O)	0,0,0	885.8	413.4	78.2
LG424	8	320.9 (O)	0,0,0	833.3	744.8	20.1
LG427	24	317.9 (O)	0,0,0	915.4	607	56.0
LG429	16	316.2 (O)	0,0,0	915.4	718.5	38.4
LG432	16	320 (O)	0,0,0	895.7	649.6	47.4
LG594	8	306.77 (N)	27.0,6.6,47.8	843.9	484.5	67.0
LG609	8	312.27 (N)	37.35,0.8,1.63	913.7	825.4	18.4
LG610	8	312.27 (N)	25.3,0.7,11.93	888.1	809.7	16.9
LG611	8	324.08 (O)	30.89,-	905.7	798.1	22.4
LG612	8	324.08 (O)	22.78,-3.74,-0.53	898.3	822.7	16.1
LG618	8	312.27 (N)	-	866.4	558.9	58.4
LG620	8	316.2 (N)	-	893.8	580.8	57.8
LG656	32	324.08 (O)	8.98,-2.31,-10.07	967.3	469.2	76.5

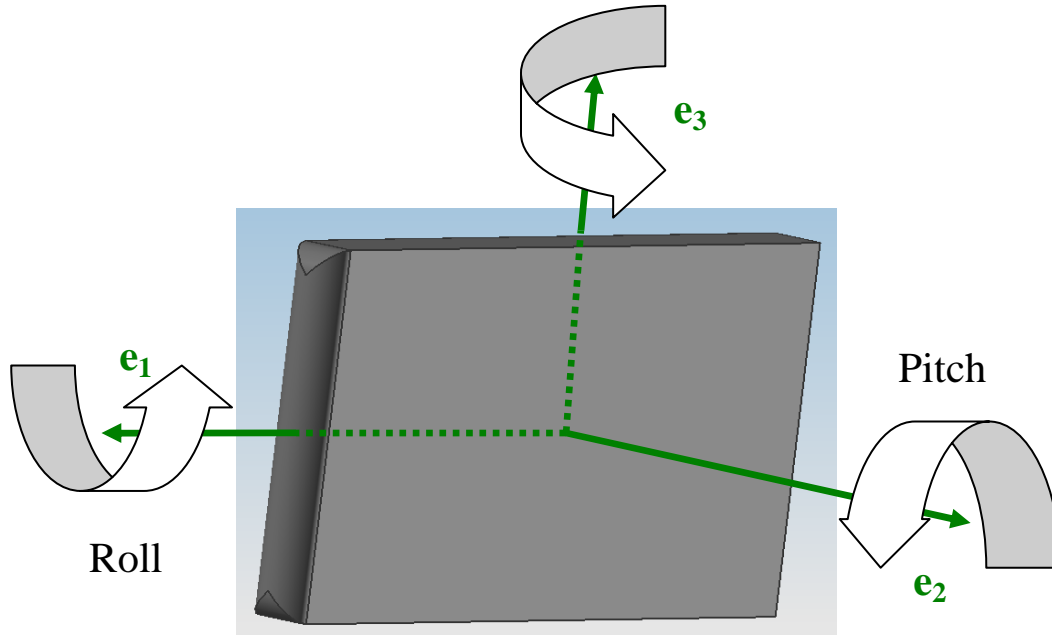|						
LG657	32	324.08 (O)	-22.16,9.73,1.42	829.7	0	100.0
LG689	8	323.24 (O)	-12.83,-	896.3	655.1	46.6
LG692	8	324.08 (O)	38.24,2.31,41.45	885.3	602.6	53.7

Figure 15. Roll, Pitch, And Yaw Angles of the Projectile

Table 2. Experimental Versus FE Model Predictions

Model	Experimental Absorbed Energy	SL Absorbed Energy Diff., D	ML Absorbed Energy Diff., D
	(%)	(%)	(%)
LG404	16.1	1.0	2.8
LG409	17.6	2.3	3.9
LG424	20.1	1.3	1.9
LG609	18.4	5.7	8.6
LG610	16.9	0.2	7.5
LG611	22.4	10.0	9.0
LG612	16.1	0.5	4.3
LG618	58.4	-5.0	-40.1
LG594	67.0	-3.5	4.9
LG620	57.8	6.6	9.5
LG689	46.6	0.9	20.5
LG692	53.7	5.7	17.9
LG429	38.4	9.1	16.4

LG432	47.4	10.0	21.8
LG411	78.2	9.0	36.9
LG427	56.0	-4.8	15.5
LG656	76.5	20.9	26.3
LG657	100.0	0.0	0.0
	Avg.	**3.9**	**9.3**
	Std. Dev.	**6.4**	**15.7**

Table 3. Ballistic Limit Prediction (direct hit)

Layers	Projectile	SL Model (ft/s)	ML Model (ft/s)
4	New	475 - 525	-
12	New	725 - 775	660 - 710
16	New	840 - 870	775 - 800
24	New	950 - 975	825 - 860
32	Old	1042 - 1083	875 - 917

Sensitivity Analysis

A sensitivity analysis of the material model was performed to determine the multi FE layer model's sensitivity to various input parameters. These parameters included the elastic modulii (E_{11} and E_{22}), the shear modulii (G_{12}, G_{23}, and G_{31}), the failure strain, the coefficient of friction and the projectile orientation. For parameters that were taken from experimental results, such as E_{11} and E_{22}, the values were adjusted by -10%, -5%, +5%, and +10%. For other parameters that were assumed in the material model, such as coefficient of friction and the failure strain, lower and higher values than the assumed values were used. All the test cases were used for the sensitivity analysis. A ranking of the parameters from the material model's highest sensitivity to lowest sensitivity based on the sensitivity analysis and from general observations during this research is as follows:

(1) E_{11}
(2) E_{22}
(3) Coefficient of friction between steel and fabric
(4) G_{12}
(5) Failure strain
(6) Coefficient of friction between fabric and fabric
(7) G_{23} and G_{31}

5.0 Concluding Remarks

The developed methodology is general enough such that it can be used for other fabrics and fabric types. Comparison of the absorbed energy and deformation patterns with experimental results show that the developed constitutive relationship, damage and failure predictions provide favorable comparisons. While not readily apparent, strain-rate dependence on Kevlar's stress-strain relationship is an important part of the model. In a rather complex model such as the one discussed in this paper, there are several parameters that can potentially affect the results. The regression analysis shows that, in general, that the model is most sensitive to any parameter which affects the area under the assumed stress-strain curves such as the elastic stiffness and the

post-peak behavior. On average, single layer models predict the ballistic performance better than multiple layer models. However, a multi layer model can capture the interaction between fabric layers and hence can determine the actual number of fabric layers that have failed in a contained simulation.

References

Gasser, A., Boisse, P. and Hanklar, S. (2000), "Mechanical behavior of dry fabric reinforcement. 3D simulations versus biaxial tests." Comp Mater Sci, 17(1):7–20.

Ishikawa, T., and Chou, T.W. (1982), "Stiffness and Strength Behavior of Woven Fabric Composites," J Compos Mater, 17:3211-220.

Jiang, Y., Tabiei, A., and Simitses, G.J. (2000), "A Novel Micromechanics-Based Approach to the Derivation of Constitutive Equations for Local/Global Analysis of Plain-Weave Fabric Composite," J Compos Sci Tech, 60: 1825-33.

Naik, D., Sankaran, S., Mobasher, B., Rajan, S.D. and Pereira, J.M. (2009). "Development of Reliable Modeling Methodologies for Fan Blade-Out Containment Analysis. Part I: Experimental Studies", J of Impact Engineering, 36:1, 1-11.

Raftenberg, M. (2004), "Modeling thoracic blunt trauma – towards a finite element-based design methodology for body armor," Technical Report, U. S. Army Research Laboratory Aberdeen Proving Ground, MD.

Scida, D. (1999), "A Micromechanics Model for 3D Elasticity and Failure of Woven-Fibre Composite Materials," J Compos Sci Tech, 59:505-17.

Stahlecker, Z., Mobasher, B., Rajan, S.D. and Pereira, J.M. (2009). "Development of Reliable Modeling Methodologies for Fan Blade-Out Containment Analysis. Part II: Finite Element Analysis", J of Impact Engineering, 36:3, 447-459.

Xia Y and Wang Y. (1999). "Experimental and theoretical study on the strain rate and temperature dependence of mechanical behavior of Kevlar fibre", Comp Part A, 30: 1251-57.